EMIRS observations of the aphelion-season Mars atmosphere

Michael D. Smith[1], Khalid Badri[2], Samuel A. Atwood[3,4], Christopher S. Edwards[5], Philip R. Christensen[6], Michael J. Wolff[7], Tanguy Bertrand[8], François Forget[9], Eman Al Tunaiji[2], Christopher Wolfe[5], Nathan Smith[5], Saadat Anwar[6]

[1]NASA Goddard Space Flight Center, Greenbelt, MD 20771, USA.

[2]Mohammed bin Rashid Space Center, Emirates Institute for Advanced Science and Technology, Al Khawaneej Area, Dubai, UAE.

[3]Space and Planetary Science Center, and Department of Earth Sciences, Khalifa University, Abu Dhabi, UAE

[4]Laboratory for Atmospheric and Space Physics, University of Colorado Boulder, Boulder, CO, USA.

[5]Department of Astronomy and Planetary Science, Northern Arizona University, Flagstaff, AZ, USA.

[6]School of Earth and Space Exploration, Arizona State University, Tempe, AZ, USA.

[7]Space Science Institute, Boulder, CO, USA

[8]Laboratoire d'Etudes Spatiales et d'Instrumentation en Astrophysique (LESIA), Observatoire de Paris, Université PSL, CNRS, Sorbonne Université, Univ. Paris Diderot, Sorbonne Paris Cité, Meudon, France

[9]LMD/IPSL, Sorbonne Université, PSL Research Université, École Normale Supérieure, École Polytechnique, CNRS, Paris, France

Corresponding author: Michael D. Smith (Michael.D.Smith@nasa.gov)

Key Points:

- Thermal infrared spectra of Mars taken by the Emirates Mars Infrared Spectrometer have been used to characterize the atmospheric state.
- These aphelion season observations show the expected relatively cool atmosphere with prominent water ice clouds and generally little dust.
- The initiation and evolution of a regional dust storm that occurred unusually early in the season was observed.

Abstract

Thermal infrared spectra taken by the Emirates Mars Infrared Spectrometer (EMIRS) on-board the Emirates Mars Mission (EMM) spacecraft are well suited for the retrieval of surface temperatures, the atmospheric temperature profile from the surface to ~40 km, and the column abundance of dust aerosols, water ice clouds, and water vapor. A constrained linear inversion retrieval routine that includes multiple scattering has been developed and optimized for this purpose. Here, we present a brief overview of the retrieval algorithm and first atmospheric science results from observations taken by EMIRS over the first Earth year of EMM Science Phase operations. These retrievals show extensive water ice clouds, typical for the aphelion season of these observations, and the expected north polar summer maximum and subsequent equatorward transport of water vapor is well documented. An unusually strong and early regional dust storm and its associated thermal response were also observed.

Plain Language Summary

Data returned from the Emirates Mars Infrared Spectrometer (EMIRS) have been used to characterize the atmosphere of Mars. These data allow estimates of atmospheric temperature as a function of height, the amount of dust and water ice clouds in the atmosphere, and the abundance of water vapor. In this work we describe the process for estimating these quantities and we give a brief overview of our first results. The results show that Mars was relatively cool, relatively cloudy, but with little dust. This was expected given the season on Mars that was observed. More surprising was the observation of a dust storm that occurred earlier in the Martian year than usual.

1 Introduction

Thermal infrared spectroscopy has proven to be an effective means for characterizing the thermal structure, aerosol optical depth, and water vapor abundance in the lower atmosphere of Mars. Numerous examples include the spectrometers on-board Mariner 9 (e.g., Conrath et al., 1975), Mars Global Surveyor (e.g., Conrath et al., 2000; Smith 2002, 2004), Mars Exploration Rovers (e.g., Smith et al., 2006), Mars Express (e.g., Fouchet et al., 2007; Giuranna et al., 2021), and the ExoMars Trace Gas Orbiter (e.g., Guerlet et al., 2022). Multiband thermal infrared instruments on-board the Viking Orbiter (e.g., Kieffer et al., 1977; Tamppari et al., 2003), Mars Odyssey (e.g., Smith, 2009, 2018), and Mars Reconnaissance Orbiter (e.g., Kleinböhl et al., 2009; McCleese et al., 2010) have provided additional important information. Useful summaries of many of these observations can be found in the review articles by Smith et al. (2017), Kahre et al. (2017), Clancy et al. (2017), and Montmessin et al. (2017).

The Emirates Mars Infrared Spectrometer (EMIRS; Edwards et al., 2021) is an instrument with direct heritage to the Thermal Emission Spectrometer (TES; Christensen et al., 2001). Beyond the value of extending the existing, multi-decadal record of continuous spacecraft observations of the Mars atmosphere, the EMIRS instrument takes advantage of the unique, high-altitude orbit of the Emirates Mars Mission (EMM; Amiri et al., 2022; Almatroushi et al., 2021), which enables sampling of all local times over a wide range of latitudes and longitudes over a short sub-seasonal timescale of less than two weeks. This ability of EMIRS is explored for water ice clouds by Atwood et al. (2022) and for thermal tides by Fan et al., (2022). Analysis of possible diurnal variations in dust optical depth and water vapor abundance is ongoing. Here, we present an overview of the retrieval algorithm used for obtaining atmospheric temperatures, dust and water ice column optical depth, and water vapor column abundance from EMIRS spectra along with a description of the results taken during the first Earth year (northern spring and summer on Mars) of daytime observations during the Science Phase of the EMM mission.

2 Data set and retrieval algorithm

2.1 EMIRS instrument and data

EMIRS is a thermal infrared spectrometer that observes Mars at wavelengths between ~100 and 1600 cm^{-1} (~100 and 6 μm) at a selectable spectral resolution of 5 or 10 cm^{-1} (Edwards et al., 2021). Most observations are taken at 10 cm^{-1}, but both spectral resolutions are used. From its 55-hour period orbit that varies between 20,000 and 43,000 km altitude, EMIRS raster scans the disk of Mars ~20 times during each orbit to provide a global, synoptic view of Mars that samples all local times, day and night. Over the course of approximately 4 orbits (or 10 days, or 5° of L_s), sufficient observations are taken to provide a broad sampling of all local times at nearly all latitudes and longitudes. The typical footprint size (~100–300 km) precludes limb-geometry observations, but this spatial resolution is comparable to that of global circulation models and is sufficient to provide a detailed global view of the current climate state.

2.2 Retrieval algorithm

The retrieval follows the constrained linear inversion algorithm of Conrath et al. (2000) and Smith et al. (2006) to retrieve atmospheric state parameters that best match the observed EMIRS spectra. Retrieved here are surface temperature, the atmospheric temperature profile from the surface to ~40 km altitude, the column extinction optical depths of dust and water ice aerosols, and the column abundance of water vapor. The forward radiative transfer model includes a discrete ordinates treatment of multiple scattering by aerosols (e.g., Goody & Yung, 1989; Thomas & Stamnes, 1999). Typically, four radiation streams (two upward and two downward) are sufficient to accurately model aerosols at these wavelengths, but this is a free parameter within the model that can be adjusted as needed. Only observations with emergence angle less than 70° are used, so the effects of spherical geometry are neglected. The model accounts for the absorptions from CO_2 and water vapor gases using the HITRAN2020 database (Gordon et al., 2022) and the correlated-k approximation (Lacis & Oinas, 1991). Coefficients for CO_2 broadening of water vapor are taken from Brown et al (2007), which includes the most important lines in the EMIRS spectral range. Other weak lines not included in Brown's work have their air-broadened value multiplied by a constant factor of 1.5.

Following Conrath et al. (2000), a smoothness constraint is applied for the temperature profile retrieval using a two-point correlation matrix with a correlation length of 0.75 scale heights, and the first-guess profile is obtained from the observed radiances. The bottom of the temperature profile (lowest ~0.75 scale heights) is constrained to have a lapse rate consistent with the Mars Climate Database (MCD; Forget et al. 1999; Millour et al., 2018), while the top of the profile above an altitude of ~4 scale heights is constrained by temperatures from the MCD.

Given that the spectral signatures of gases and aerosols are relatively well separated in the spectral range observed by EMIRS, the retrieval is performed sequentially. First, surface temperature and the atmospheric temperature profile is retrieved using the strong CO_2 absorption centered at 667 cm^{-1} (15 μm). Next, the column optical depths of dust and water ice aerosol are retrieved along with a refinement of surface temperature using a large portion of the EMIRS spectrum between 250 and 1315 cm^{-1} (excluding the CO_2 band). Finally, the column abundance of water vapor is retrieved using the rotation bands between 200 and 350 cm^{-1}. This sequence can be iterated to obtain a self-consistent solution, with the entire process completing in less than a second on a desktop computer.

There are a number of assumptions that must be made to perform the retrieval. The surface pressure cannot be reliably retrieved with the EMIRS data alone, and so it is instead taken from the MCD for the given L_s, latitude, longitude, local time, and size of the EMIRS field of view on the surface for each observation. Aerosol optical properties are taken from Wolff et al. (2006), with aerosol effective radii of 1.5 µm for dust and 2.0 µm for water ice to be consistent with previous retrievals (e.g., Smith 2004; 2019). The vertical distribution of dust is assumed to follow a Conrath profile (Conrath, 1975). The Conrath-ν parameter is chosen so that the top of the dust layer varies as a function of season and latitude ranging from 1 (aphelion, high latitudes) to 5 scale heights (perihelion, low latitudes) based on prior observations (e.g., Heavens et al., 2011; Smith et al., 2013). Water ice clouds are placed at the water condensation level, while water vapor is well-mixed up to its condensation level, which is computed using the retrieved temperature profile and water vapor column. Surface emissivity is taken from a map derived from TES observations (Smith et al., 2000; 2003; Bandfield, 2002).

2.3 Uncertainties

Uncertainties in retrieved quantities come from a combination of random noise in the observed radiance and systematics in the retrieval. Usually, the retrieval uncertainties from random noise are relatively small and our retrieval uncertainty is dominated by the assumptions and approximations of the retrieval algorithm. We characterize these using numerical experiments, for example, by changing the number of radiation streams in the radiative transfer model or modifying the vertical distribution of the aerosols to evaluate their effect on the retrieved parameters. We estimate the uncertainty in surface temperature at 1 K, and the uncertainty in atmospheric temperatures to be 2 K at altitudes between 1 and 3 scale heights above the surface, but larger (approaching 5–10 K) in the lowest scale height and at higher altitudes. The vertical resolution of the atmospheric temperature profile is roughly 1–1.5 scale heights, consistent with the width of the CO_2 contribution functions (e.g., Conrath et al., 2000).

In these nadir geometry observations, a thermal contrast between the surface and the atmosphere is required to observe the absorption (or emission) features from dust, water ice clouds, and water vapor. This thermal contrast becomes vanishingly small near dawn and dusk, which limits our ability to perform the aerosol and water vapor retrievals at those local times. The uncertainty in retrieved parameters is directly related to the amount of thermal contrast, so we compute an estimate for the uncertainty in each retrieved parameter for every retrieval since this uncertainty varies greatly with season, latitude, and local time (Edwards et al., 2021). In practice, for the daytime retrievals presented in this work, we retain only those retrievals for dust and water ice optical depth with uncertainty less than 0.05 (although most have uncertainties in the 0.01–0.03 range). And similarly, the uncertainty in the water vapor retrievals is less than 5 pr-µm for the results presented here.

3 Results

EMIRS has operated almost continuously since the beginning of EMM Science Phase on 24 May 2021 (Mars Year or MY 36, L_s=49°). Included here are retrievals from observations taken during Science Phase through 24 February 2022 (MY 36, L_s=180°). During that period EMIRS took more than 1500 images of Mars including more than 270,000 retrievable observations (with the EMIRS field of view on the disk of Mars and an emergence angle of less than 70°).

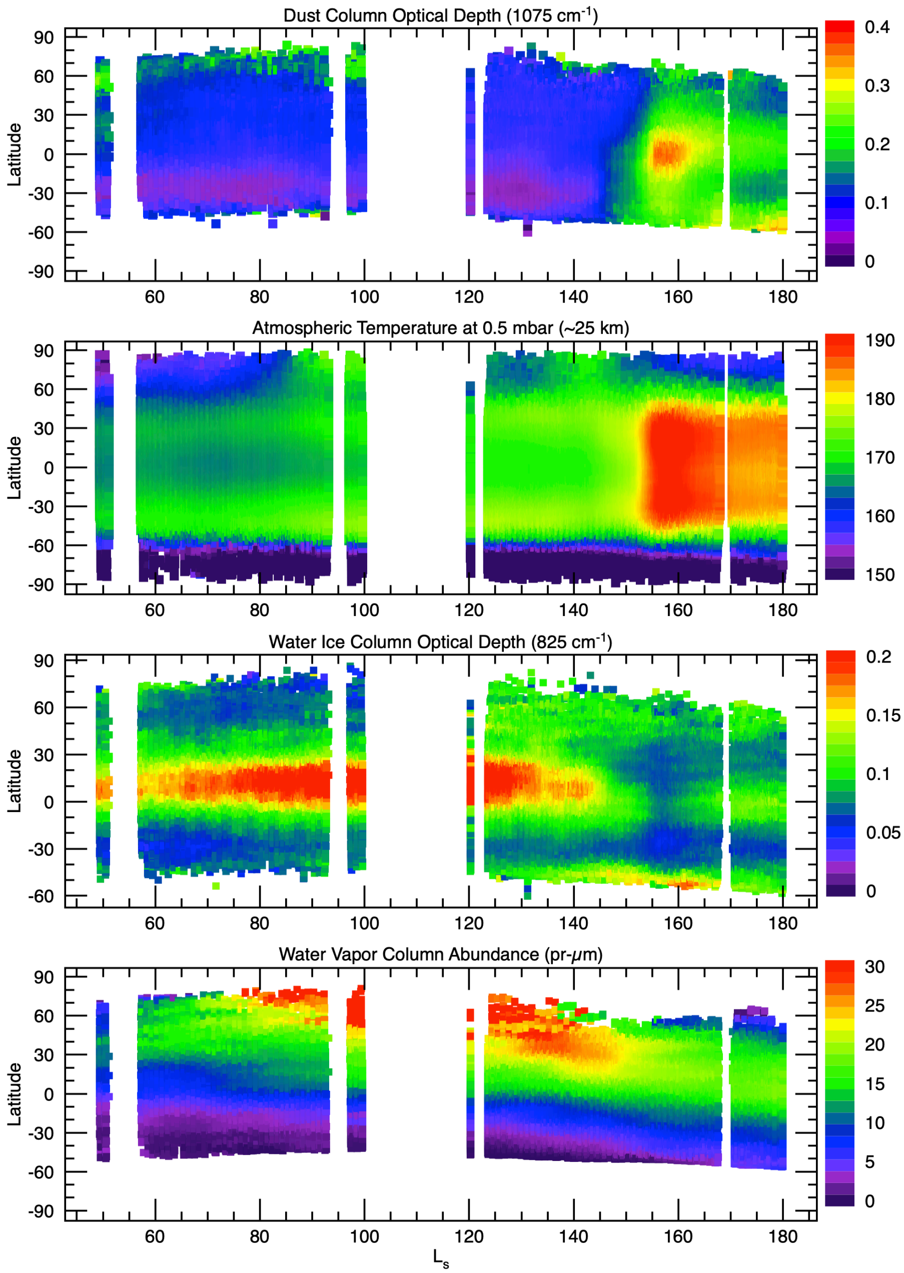

Figure 1: The seasonal and latitudinal variation of **(a)** dust column-integrated optical depth, **(b)** atmospheric temperature at 0.5 mbar (~25 km), **(c)** water ice cloud column-integrated optical depth, and **(d)** water vapor column abundance (pr-µm) as retrieved from EMIRS daytime (~07:00–18:00) observations.

3.1 Overall climatology

Figure 1 provides an overview of the retrieval results for EMIRS observations taken between 24 May 2021 (MY 36, L_s=49°) and 24 February 2022 (MY 36, L_s=180°). The gap between

L_s=100° and 120° was caused by the combination of solar conjunction and the spacecraft entering safe mode. Shown are zonal daytime averages of dust extinction column optical depth (referenced to 1075 cm^{-1} or 9 μm), daytime atmospheric temperature (at 0.5 mbar or ~25 km altitude), daytime water ice cloud extinction column optical depth (referenced to 825 cm^{-1} or 12 μm), and the daytime column abundance of water vapor (pr-μm). In each case the retrieval results have been smoothed with a box 5° in L_s and 2° in latitude to ensure that there is a representative sample of longitudes in the zonal average.

The expected aphelion-season variations and interrelations between the four quantities (e.g., Smith, 2004) are evident in Fig. 1. Dust exhibits its annual minimum optical depth during this season with retrieved 9-μm dust optical depths near 0.1. Higher dust opacity (0.2–0.3) was observed at high northern latitudes, consistent with the greater local dust storm activity observed along the retreating edge of the polar cap (e.g., Cantor et al., 2001). Latitude/longitude maps show dust opacity correlating with surface pressure, with higher dust columns in the lower topography regions. The rise of dust optical depth at L_s=145° signaled a return of greater dust activity planetwide, with the occurrence of a relatively strong early season regional dust storm beginning at L_s=151°. As northern autumn equinox (L_s=180°) and the traditional start of the "dust storm season" approached, the observed dust optical depth was generally on the rise, especially in the south.

Atmospheric temperatures were cool in the south (winter) hemisphere and gradually warmed at all latitudes as Mars moved away from aphelion (L_s=71°). A much more rapid warming was observed as a response to the additional airborne dust during the regional dust storm, with temperatures gradually cooling as dust from the regional storm settled out of the atmosphere. The latitudinal structure of atmospheric temperatures at this height, with relative maxima at mid latitudes in each hemisphere is indicative of the general circulation pattern with downward motion at those latitudes.

The low-latitude aphelion season water ice cloud belt dominated the retrievals of clouds during this period with additional polar clouds appearing later in the season (Atwood et al., 2022). Water ice cloud optical depth in the aphelion cloud belt reached a maximum between L_s=100° and 120° and decreased significantly after L_s=130°. Cloud opacity was significantly diminished during the regional dust storm, with equatorial clouds returning after the peak of the dust storm. At higher latitudes, clouds became more common in both hemispheres later in the season after L_s=120°.

Finally, the retrievals clearly show a high-latitude northern hemisphere summer maximum in water vapor abundance and the subsequent equatorward transport of water vapor during Northern Hemisphere summer. Water vapor abundance increased rapidly at high northern latitudes during spring reaching peak values sometime after solstice. Maximum retrieved water vapor columns were greater than 30 pr-μm, although the peak was likely missed because of the lack of retrievals between L_s=100° and 120° and the difficulty of observing the pole from the low-inclination orbit of EMM. After L_s=120°, the latitudinal maximum of water vapor migrated southward and diminished as water was transported equatorward by the general circulation. By L_s=180°, the maximum water vapor column was about 15 pr-μm in a band centered just north of the equator. The regional dust storm appeared to have no significant effect on retrieved water vapor abundance.

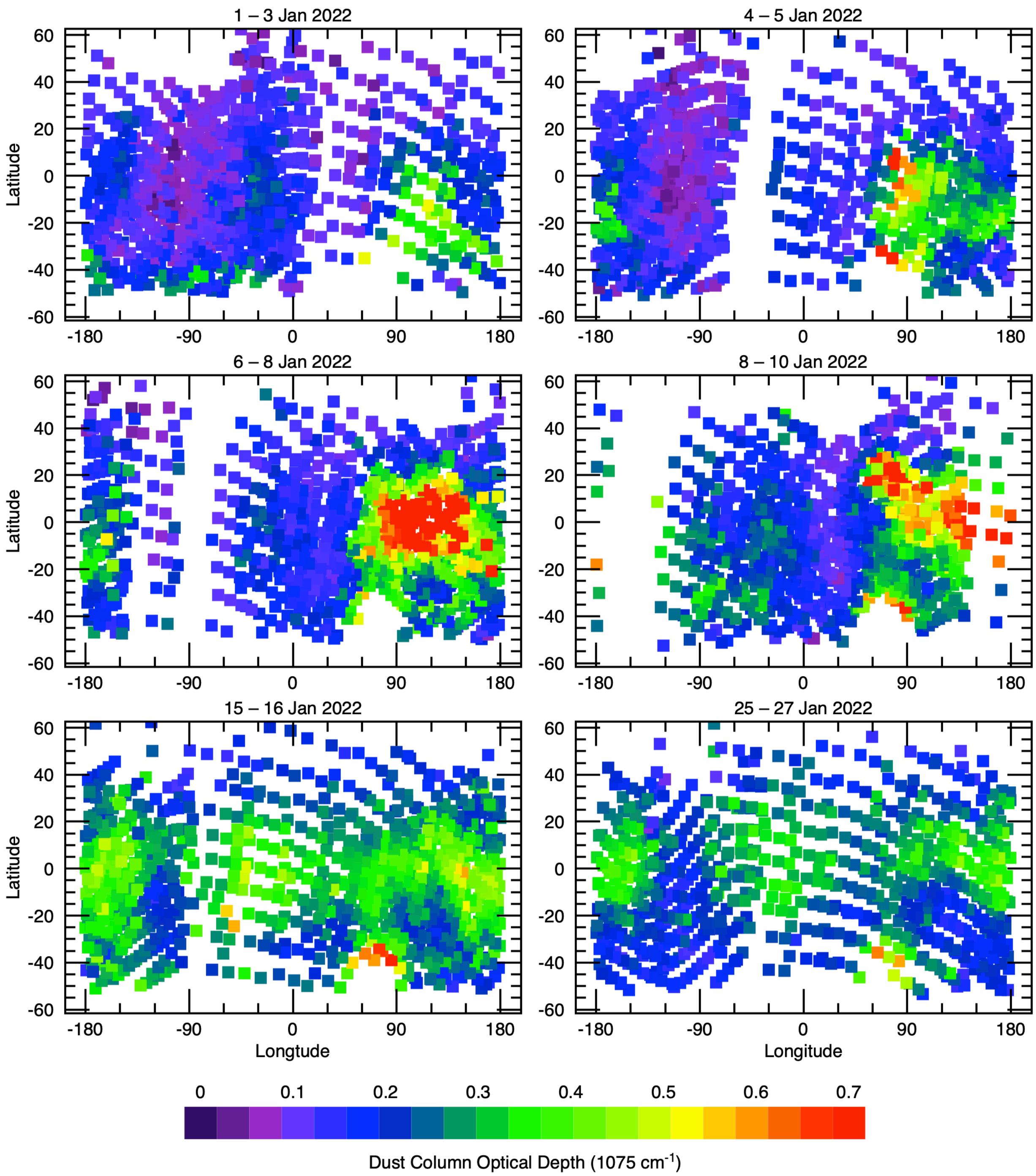

Figure 2: Maps of 9-μm dust optical depth retrieved from EMIRS observations showing the initiation, growth, and decay of a regional dust storm. Each point on the map represents an individual EMIRS retrieval and there is no smoothing or scaling for topography performed. The season covered here is from L_s=151°–164°.

3.2 Regional dust storm

Figure 2 shows the initiation, growth, and decay of a regional dust storm observed by EMIRS. Each point in the figures shows an individual EMIRS retrieval without any further smoothing and without scaling for topography. The active portion of the dust storm occurred during roughly the first two weeks of January 2022 (MY 36, L_s~151°–160°). Dust activity was initially concentrated at mid-southern latitudes between 90° and 180° E longitude (north and east of Hellas Planitia). Over the period of several days, that localized activity rapidly developed into a regional-scale dust storm spreading northward into low latitudes in the same longitude band carried by the return branch of the Hadley cell circulation. At its peak intensity between 6 and 8 January 2022 (L_s=154°), retrieved 9-μm dust optical depths of 0.7 or greater were recorded over a large region centered near the equator covering 30° in latitude and 90° in longitude. Isolated retrievals within the core of the dust storm indicated dust optical depth exceeding unity.

Although regional dust storms during this season are unusual, similar storms have been observed during MY 27, 29, and 32 (Battalio & Wang, 2021). Usually, such storms are produced by tide activity in the southern hemisphere, locally increasing the surface stress in the region of Hellas (particularly at its northern and eastern edges), thus favoring increased dust lifting when dust is available. At this season (L_s=150°), climate models (e.g., the MCD; Forget et al. (1999)) predict a relatively weak return branch of the Hadley cell in the southern hemisphere, but non-uniform in longitude. At the longitudes just east of Hellas, the meridional winds are relatively strong, which enhances the ability of local dust storms in this region to quickly spread northward and grow to regional scale as observed by EMIRS.

After the main active portion of the storm ended, little new dust was lofted into the atmosphere. The dust that had already been lofted was advected eastward by the general circulation over the next week reaching all longitudes by 15 January 2022 (L_s=158°). Dust opacity remained elevated (~0.4) at low latitudes (-30° to +30°) at this time, although there was significant clearing at higher southern latitudes with optical depth values falling back to ~0.2. Retrieved dust optical depth continued to slowly decrease through the end of January (last panel in Fig. 2, L_s=164°) and the rest of northern summer as dust settled out, although it never reached the low, pre-dust storm levels. A significant exception to this general trend was observed in Hellas Planitia, which remained active and filled with dust throughout this period.

3.3 Temperature cross-sections

Figure 3 shows atmospheric temperature cross-sections retrieved from EMIRS afternoon observations (12:00–16:00 LTST) for three different seasons, at Northern Hemisphere summer solstice (L_s=85°–95°), Northern Hemisphere mid-summer (L_s=140°–150°), and just a few weeks later during the regional dust storm described above (L_s=155°–165°). Here, zonal mean cross-sections have been produced by smoothing all the individual temperature profiles using a box 5° wide in latitude.

For the first two cases the retrieved thermal structure of the atmosphere is typical for this aphelion season (e.g., Smith 2004; McCleese et al., 2010). In this season, solar heating is maximum in the northern (summer) hemisphere and the latitudinal temperature gradients are relatively small. In the southern (winter) hemisphere temperatures can reach the CO_2 frost point close to the pole. Adiabatic heating caused by the downward motion of a cross-equatorial Hadley circulation produces a warmer region aloft that overlies the coldest air near the pole and forms a polar front with a characteristic tilt with the latitude of the maximum temperature moving away from the pole as the height becomes closer to the surface.

Atmospheric temperatures are heavily modified by dynamical processes and tides (e.g., Fan et al., 2022) and the radiative effects of aerosols (e.g., Gierasch and Goody, 1972). The effect of direct heating of the atmosphere from dust is apparent when comparing the two lower panels in Fig. 3, showing the retrieved thermal structure just before and during the regional dust storm. Daytime temperatures at 0.5 mbar (~25 km) and higher above the surface were roughly 20 K warmer at the peak of the dust storm compared to just before the storm. On the other hand, atmospheric temperatures near the surface remained similar, and surface temperatures cooled during the dust storm, an effect observed previously by TES and other instruments (e.g., Smith et al., 2002; Kleinböhl et al., 2020; Wolkenberg et al., 2020).

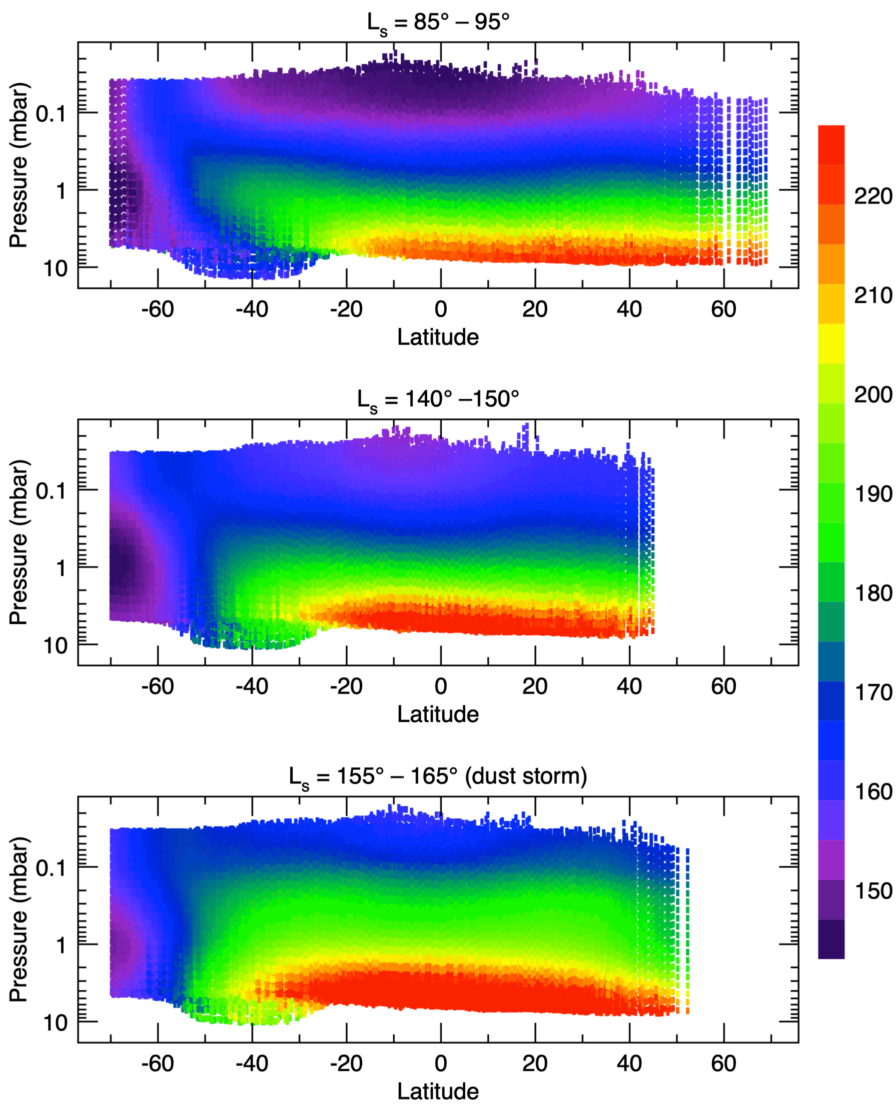

Figure 3: Latitude-pressure cross-sections of daytime (12:00–16:00 LTST) atmospheric temperatures retrieved from EMIRS observations for three different seasons: **(a)** L_s=85°–95° at northern hemisphere solstice, **(b)** L_s=140°–150°, just before a regional dust storm, and **(c)** L_s=155°–165° during the regional dust storm.

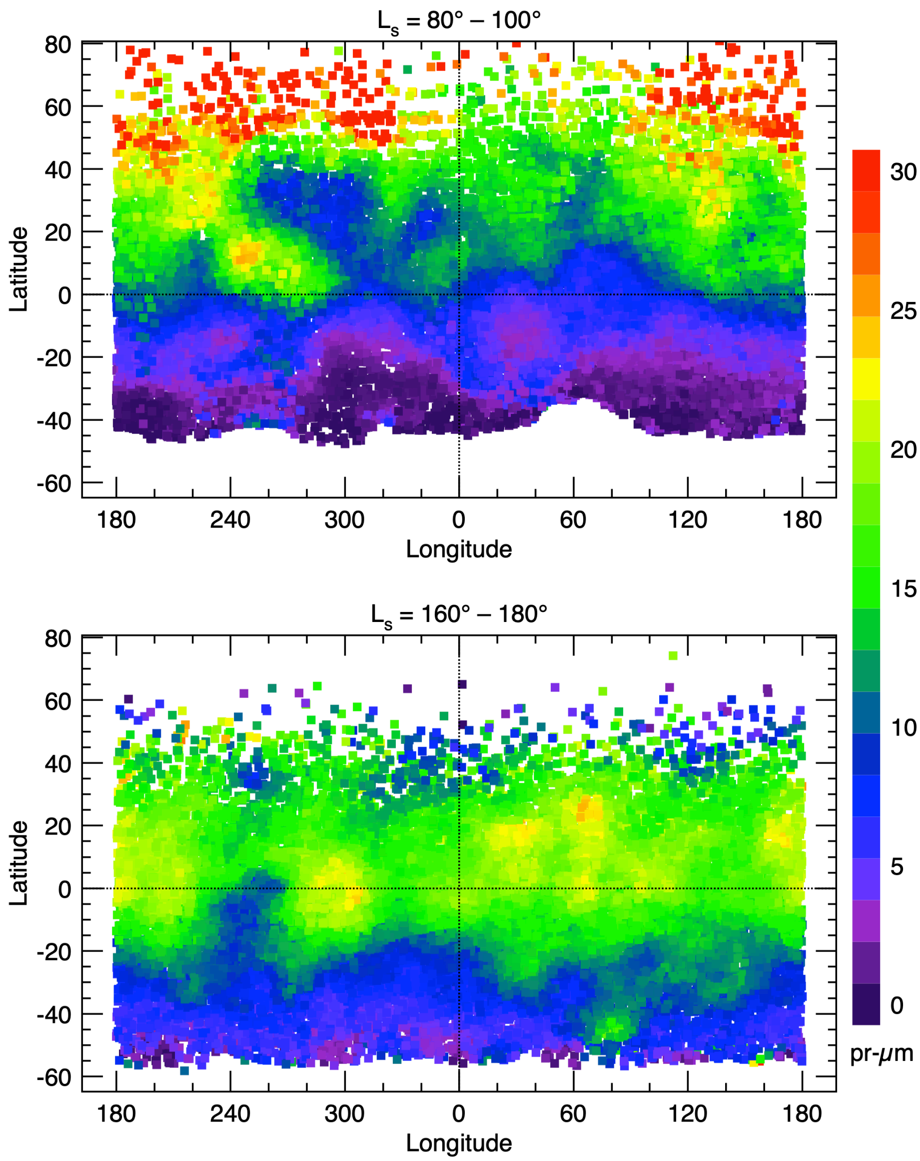

Figure 4: Maps of the column abundance of water vapor retrieved from EMIRS observations for two seasons: **(a)** L_s=80°–100° at northern hemisphere solstice, and **(b)** L_s=160°–180° at the end of northern summer. There has been no scaling for topography performed here.

3.4 Water vapor

Maps of the column abundance of water vapor retrieved from EMIRS observations are shown in Fig. 4. In these maps, there is no scaling for topography, but the results have been smoothed with a box 10° in latitude by 20° in longitude to better show spatial features. The strong north-to-south gradient in water vapor typical of northern summer solstice (e.g., Jakosky & Farmer, 1982; Smith 2002; Trokhimovskiy et al., 2015; Smith et al., 2018) is evident in the top panel as water sublimed from the seasonal polar cap. The retrieved water vapor columns exceeded 30 pr-µm at high northern latitudes. The longitude dependence of water vapor was correlated with topography implying that water vapor was mixed to high enough altitudes that a greater atmospheric column led to a greater water vapor column. There was also a weaker positive correlation with the spatial dependence of surface albedo and negative correlation with thermal inertia implying that surface interactions may play a role in the distribution of water vapor. The southern (winter) hemisphere was quite dry with retrieved water vapor columns less than 5 pr-µm poleward of -30° latitude.

Near equinox (lower panel of Fig. 4), the EMIRS retrievals show that the maximum water vapor column had migrated southward to just north of the equator, with a zonally averaged value near 15 pr-µm. Compared to the solstice season, water vapor also gradually increased in the southern hemisphere with column abundances of 5–10 pr–µm at mid-southern latitudes. Longitude variations and the associated correlations with topography, albedo, and thermal inertia appeared weaker at this season than during the solstice season.

4 Conclusions and summary

EMIRS thermal infrared spectra are well suited for the retrieval of atmospheric temperature profiles and the column-integrated quantities of dust and water ice aerosol optical depth and of water vapor abundance, while the unique orbit of EMM enables nearly the entire atmosphere of Mars to be sampled over all local times on timescales of ~10 days. The thermal structure and the spatial variations of aerosols and water vapor were mostly as expected for the observed aphelion season. Dust opacity was near its annual minimum and had a latitudinal gradient with more dust in the northern hemisphere. An unusually early regional dust storm peaked at L_s=154° with dust optical depth exceeding unity in its core at its peak intensity. Atmospheric temperatures were relatively cool, especially in the winter hemisphere, and gradually warmed as Mars moved away from aphelion. Atmospheric temperatures increased significantly, by ~20 K, in response to the regional dust storm. Water ice clouds were plentiful, with the typical aphelion-season low-latitude belt apparent and extensive clouds at high northern and southern latitudes after L_s=120°. The annual maximum abundance of water vapor was observed at high northern latitudes near summer solstice. That water vapor was observed to be transported equatorward during northern summer. Clear diurnal variations in atmospheric temperatures and water ice cloud opacity were evident in the retrievals (Atwood et al., 2022; Fan et al., 2022). Detailed analysis of these retrieval results, especially in conjunction with results obtained from the two other instruments on-board EMM, the Emirates Exploration Imager (Jones et al., 2021) and the Emirates Mars Ultraviolet Spectrometer (Holsclaw et al., 2021), will improve our understanding of the underlying physical processes that operate in the current Mars atmosphere, while also helping to validate and tune general circulation models. Systematic EMIRS observations continue as the part of the baseline set of ongoing EMM mission activities promising exciting new information as we enter the dusty perihelion season.

Acknowledgments

Funding for development of the EMM mission was provided by the UAE government, and to co-authors outside of the UAE by the Mohammed bin Rashid Space Center (MBRSC). SAA acknowledges funding through the grant 8474000332-KU-CU-LASP Space Sci.

Data availability

Data from the Emirates Mars Mission (EMM) are freely and publicly available on the EMM Science Data Center (SDC, http://sdc.emiratesmarsmission.ae). This location is designated as the primary repository for all data products produced by the EMM team and is designated as long-term repository as required by the UAE Space Agency. The data available (http://sdc.emiratesmarsmission.ae/data) include ancillary spacecraft data, instrument telemetry, Level 1 (raw instrument data), Level 2 (calibrated radiance spectra), Level 3 (derived science products), quicklook products, and data users guides (https://sdc.emiratesmarsmission.ae/documentation) to assist in the analysis of the data.

Following the creation of a free login, all EMM data are searchable via parameters such as product file name, solar longitude, acquisition time, sub-spacecraft latitude & longitude, instrument, data product level, etc.

Data products can be browsed within the SDC via a standardized file system structure that follows the convention:

/emm/data/<Instrument>/<DataLevel>/<Mode>/<Year>/<Month>

Data product filenames follow a standard convention:

emm_<Instrument>_<DataLevel><StartTimeUTC>_<OrbitNumber>_<Mode>_<Description>_ <KernelLevel>_<Version>.<FileType>)

EMIRS data and user's guides are available at: https://sdc.emiratesmarsmission.ae/data/emirs

References

Almatroushi, H., AlMazmi, H., AlMheiri, N., et al. (2021), Emirates Mars Mission characterization of Mars atmosphere and dynamics and processes, Space Sci. Rev. 217:89, doi:10.1007/s11214-021-00851-6.

Amiri, H.E. S., Brain, D., Sharaf, O., et al. (2022), The Emirates Mars Mission, Space Sci. Rev. 218:4, doi:10.1007/s11214-021-00868-x.

Atwood, S.A., Smith, M.D., Badri, K., Edwards, C.S., Christensen, P.R., Wolff, M.J., Forget, F., Anwar, S., Smith, N. (2022), Diurnal variability in EMIRS daytime observations of water ice clouds during Mars aphelion season, Geophys. Res. Lett., in this special issue.

Bandfield, J.L. (2002), Global mineral distributions on Mars. J. Geophys. Res. 107, E6, doi:10.1029/2001JE001510.

Battalio, M., Wang, H. (2021), The Mars Dust Activity Database (MDAD): A comprehensive statistical study of dust storm sequences, Icarus 354, 114059, doi:10.1016/j.icarus.2020.114059.

Brown, L.R., Humphrey, C.M., Gamache, R.R. (2007), CO_2-broadened water in the pure rotation and v2 fundamental regions, J. Molecular Spectrosc. 246, 1–21, doi:10.1016/j.jms.2007.07.010.

Cantor, B.A., James, P.B., Caplinger, M., Wolff, M.J. (2001), Martian dust storms: 1999 Mars Orbiter Camera, J. Geophys. Res. 106, E10, 23653–23687.

Clancy, R.T., Montmessin, F., Benson, J., Daerden, F., Colaprete, A., Wolff, M.J. (2017), Mars clouds, Chapter 5 in “The Atmosphere and Climate of Mars”, Cambridge University Press, doi:10.1017/9781139060172.005.

Christensen, P.R., Bandfield, J.L., Hamilton, V.E., et al. (2001), Mars Global Surveyor Thermal Emission Spectrometer experiment: Investigation description and surface science results, J. Geophys. Res. 106, E10, 23823–23871.

Conrath, B.J. (1975), Thermal structure of the Martian atmosphere during the dissipation of the dust storm of 1971, Icarus 24, 36–46.

Conrath, B.J., Pearl, J.C., Smith, M.D., et al. (2000), Mars Global Surveyor Thermal Emission Spectrometer (TES) observations: Atmospheric temperatures during aerobraking and science phasing, J. Geophys. Res. 105, E4, 9509–9519.

Edwards, C. S., Christensen, P. R., Mehall, G. L. et al. (2021), The Emirates Mars Mission (EMM) Emirates Mars InfraRed Spectrometer (EMIRS) Instrument. Space Sci. Rev. 217, 77. doi:10.1007/s11214-021-00848-1.

Fan, S., Forget, F., Smith, M.D., Guerlet, S., Badri, K.M., Atwood, S.A., Young, R.M.B., Edwards, C.S., Christensen, P.R., Deighan, J., Almatroushi, H.R., Bierjon, A., Liu, J., Millour, E. (2022), Migrating thermal tides in the Martian atmosphere during aphelion season observed by EMM/EMIRS, Geophys. Res. Lett., in this special issue.

Forget, F., Hourdin, F., Fournier, R., Hourdin, C., Talagrand, O., Collins, M., Lewis, S.R., Read, P.L., Huot, J.-P. (1999), Improved general circulation models of the Martian atmosphere from the surface to above 80 km, J. Geophys. Res. 104, E10, 24155–24175.

Fouchet, T., Lellouch, E., Ignatiev, N.I., Forget, F., Titov, D.V., Tschimmel, M., Montmessin, F., Formisano, V., Giuranna, M., Maturili, A., Encrenaz, T. (2007), Martian water vapor: Mars Express PFS/LW observations, Icarus 190, 32–49, doi:10.1016/j.icarus.2007.03.003.

Gierasch, P.J., and Goody, R.M. (1972), The effect of dust on the temperature of the Martian atmosphere, J. Atmos. Sci. 29, 400–402.

Giuranna, M., Wolkenberg, P., Grassi, D., Aronica, A., Aoki, S., Scaccabarozzi, D., Saggin, B., Formisano, V. (2021), The current weather and climate of Mars: 12 years of atmospheric monitoring by the Planetary Fourier Spectrometer on Mars Express, Icarus 353, 113406, doi:10.1016/j.icarus.2019.113406.

Goody, R.M., and Yung, Y.L. (1989), Atmospheric Radiation: Theoretical Basis, 2nd ed., Oxford Univ. Press, New York.

Gordon, I.E., Rothman, L.S., Hargreaves, R.J., et al. (2022), The HITRAN2020 molecular spectroscopic database, J. Quant. Spectrosc. Rad. Transf. 277, 107949, doi:10.1016/j.jqsrt.2021.107949.

Guerlet, S., Ignatiev, N., Forget, F., et al. (2022), Thermal structure and aerosols in Mars' atmosphere from TIRVIM/ACS onboard the ExoMars Trace Gas Orbiter: Validation of the retrieval algorithm, J. Geophys. Res., 127, e2021JE007062, doi:10.1029/2021JE007062.

Heavens, N.G., Richardson, M.I., Kleinböhl, A., Kass, D.M., McCleese, D.J., Abdou, W., Benson, J.L., Schofield, J.T., Shirley, J.H., Wolkenberg, P.M. (2011), The vertical distribution of dust in the Martian atmosphere during northern spring and summer: Observations by the Mars Climate Sounder and analysis of zonal average vertical dust profiles, J. Geophys. Res. 116, E04003, doi:10.1029/2010JE003691.

Holsclaw, G.M., Dieghan, J., Almatroushi, H., et al. (2021), The Emirates Mars Ultraviolt Spectrometer (EMUS) for the EMM mission, Space Sci. Rev. 217:79, doi:10.1007/s11214-021-00854-3.

Jakosky, B.M. and Farmer, C.B. (1982), The seasonal and global behavior of water vapor in the Mars atmosphere: Complete global results of the Viking atmospheric water detector experiment, J. Geophys. Res. 87, 2999–3019.

Jones, A.R., Wolff, M.J., Alshamsi, M., et al. (2021), The Emirates Exploration Imager (EXI) instrument on the Emirates Mars Mission (EMM) Hope mission, Space Sci. Rev. 217:81, doi:10.1007/s11214-021-00852-5.

Kieffer, H.H., Martin, T.Z., Peterfreund, A.R., Jakosky, B.M., Miner, E.D., Palluconi, F.D. (1977), Thermal and albedo mapping of Mars during the Viking primary mission. J. Geophys. Res. 82, 4249–4292.

Kleinböhl, A., Schofield, J.T., Kass, D.M., et al. (2009), Mars Climate Sounder limb profile retrieval of atmospheric temperature, pressure, and dust and water ice opacity, J. Geophys. Res. 114, E10006, doi:10.1029/2009JE003358.

Kleinböhl, A., Spiga, A., Kass, D.M., Shirley, J.H., Millour, E., Montabone, L., Forget, F. (2020), Diurnal variations of dust during the 2018 global dust storm observed by the Mars Climate Sounder, J. Geophys. Res. 125, e2019JE006115, doi:10.1029/2019JE006115.

Lacis, A.A. and Oinas, V. (1991), A description of the correlated k distribution method for modeling nongray gaseous absorption, thermal emission, and multiple scattering in vertically inhomogeneous atmospheres, J. Geophys. Res. 96, D5, 9027–9063.

McCleese, D.J., Heavens, N.G., Schofield, J.T., et al. (2010), Structure and dynamics of the Martian lower and middle atmosphere as observed by the Mars Climate Sounder: Seasonal variations in zonal mean temperature, dust, and water ice aerosols, J. Geophys. Res. 115, E12016, doi:10.1029/2010JE003677.

Millour, E., Forget, F., Spiga, A. et al. (2018), The Mars Climate Database (version 5.3), Scientific workshop "From Mars Express to ExoMars", ESAC Madrid, Spain.

Montmessin, F., Smith, M.D., Langevin, Y., Mellon, M.T., Fedorova, A. (2017), The water cycle, Chapter 11 in "The Atmosphere and Climate of Mars", Cambridge University Press, doi:10.1017/9781139060172.011.

Smith, M.D. (2002), The annual cycle of water vapor on Mars as observed by the Thermal Emission Spectrometer, J. Geophys. Res. 107, E11, 5115, doi:10.1029/2001JE001522.

Smith, M.D. (2004), Interannual variability in TES atmospheric observations of Mars during 1999–2003, Icarus 167, 148–165. doi :10.1016/j.icarus.2003.09.010.

Smith, M.D. (2009), THEMIS observations of Mars aerosol optical depth from 2002–2008, Icarus 202, 444–452, doi :10.1016/j.icarus.2009.03.027.

Smith, M.D. (2019), THEMIS observations of the 2018 Mars global dust storm, J. Geophys. Res. Planets 124, doi:10.1029/2019JE006107.

Smith, M.D., Bandfield, J.L., Christensen, P.R. (2000), Separation of atmospheric and surface spectral features in Mars Global Surveyor Thermal Emission Spectrometer (TES) spectra, J. Geophys. Res. 105, E4, 9589–9607.

Smith, M.D., Conrath, B.J., Pearl, J.C., Christensen, P.R. (2002), Thermal Emission Spectrometer observations of Martian planet-encircling dust storm 2001A, Icarus 157, 259–263, doi:10.1006/j.icarus.2001.6797.

Smith, M.D., Bandfield, J.L., Christensen, P.R., Richardson, M.I. (2003), Thermal Emission Imaging System (THEMIS) infrared observations of atmospheric dust and water ice cloud optical depth, J. Geophys. Res. 108, E11, 5115, doi:10.1029/2003JE002115.

Smith, M.D., Wolff, M.J., Spanovich, N., Ghosh, A., Banfield, D., Christensen, P.R., Landis, G.A., Squyres, S.W. (2006), One Marian year of atmospheric observations using MER Mini-TES, J. Geophys. Res. 111, E12S13, doi:10.1029/2006JE002770.

Smith, M.D., Wolff, M.J., Clancy, R.T., Kleinböhl, A., Murchie, S.L. (2013), Vertical distribution of dust and water ice aerosols from CRISM limb-geometry observations, J. Geophys. Res. 118, 321–334. doi:10.1002/jgre.20047.

Smith, M.D., Bougher, S.W., Encrenaz, T. Forget, F., Kleinböhl, A. (2017), Thermal structure and composition, Chapter 4 in "The Atmosphere and Climate of Mars", Cambridge University Press, doi:10.1017/9781139060172.004.

Smith, M.D., Daerden, F., Neary, L., Khayat, A. (2018), The climatology of carbon monoxide and water vapor on Mars as observed by CRISM and modeled by the GEM-Mars general circulation model, Icarus 301, 117–131, doi:10.1016/j.icarus.2017.09.027.

Tamppari, L.K., Zurek, R.W., Paige, D.A. (2003), Viking-era diurnal water-ice clouds, J. Geophys. Res. 108, E7, 5073, doi:10.1029/2002JE001911.

Thomas, G.E., and Stamnes, K. (1999), Radiative Transfer in the Atmosphere and Ocean, Cambridge Univ. Press, New York.

Trokhimovskiy, A., Fedorova, A., Korablev, O., Montmessin, F., Bertaux, J.-L., Rodin, A., Smith, M.D. (2015), Mars' water vapor mapping by the SPICAM IR spectrometer: Five martian years of observations, Icarus 251, 50–64, doi:10.1016/j.icarus.2014.10.007.

Wolff, M.J., Smith, M.D., Clancy, R.T., Spanovich, N., Whitney, B.A., Lemmon, M.T., Bandfield, J.L., Banfield, D., Ghosh, A., Landis, G., Christensen, P.R., Bell III, J.F., Squyres, S.W. (2006), Constraints on dust aerosols from the Mars Exploration Rovers using MGS overflights and Mini-TES, J. Geophys. Res. 111, E12S17, doi:10.1029/2006JE002786.

Wolkenberg, P., Giuranna, M., Smith, M.D., Grassi, D., Amoroso, M. (2020), Similarities and differences of global dust storms in MY 25, 28, and 34, J. Geophys. Res. 125, e2019JE006104, doi:10.10.29/2019JE006104.